

## Article

# Heterogeneous Activation of Persulfate by Petal-Shaped $\text{Co}_3\text{O}_4@\text{BiOI}$ to Degrade Bisphenol AF

Jian Zhang <sup>1,\*</sup>, Changling Liu <sup>1,2</sup>, Zheng Lin <sup>1</sup> and Qiang Chen <sup>1</sup>

<sup>1</sup> Chengdu Engineering Corporation Ltd., Power China, Chengdu 611130, China; liuchangling\_2011@163.com (C.L.); lin08222024@163.com (Z.L.); 2004009@chidi.com.cn (Q.C.)

<sup>2</sup> State Key Laboratory of Hydraulics and Mountain River Engineering, Sichuan University, Chengdu 610065, China

\* Correspondence: zhangjian\_202408@163.com; Tel.: +86-28-6015-8920

**Abstract:** In catalytic tests, the results have shown that almost all the BPAF was removed within 30 min when the dosage of  $\text{Co}_3\text{O}_4@\text{BiOI}$  and sodium persulfate (PS) was 0.15 g and 0.1 mM, respectively. Acid conditions inhibited BPAF degradation, but the inclusion of a precise concentration of bicarbonate ions ( $\text{HCO}_3^-$ ) promoted degradation. The presence of chloride ( $\text{Cl}^-$ ), sulfate ions ( $\text{SO}_4^{2-}$ ), and a high concentration of  $\text{HCO}_3^-$  inhibited the degradation process, whereas the addition of nitrate ions ( $\text{NO}_3^-$ ) had a minor effect on the catalytic process. The presence of free radicals (sulfate ( $\text{SO}_4^{\bullet-}$ ), hydroxyl ( $\bullet\text{OH}$ ), and superoxide ( $\text{O}_2^{\bullet-}$ )) and the non-free radical singlet oxygen ( $^1\text{O}_2$ ) in the  $\text{Co}_3\text{O}_4@\text{BiOI}/\text{PS}$  system was determined by electron paramagnetic resonance (EPR) and quenching tests. We propose that the Co(II)/Co(III) and Bi(III)/Bi(V) redox pairs simultaneously activate PS where the  $\text{Co}_3\text{O}_4$  and BiOI components work synergistically to promote the rapid oxidative degradation of BPAF in water.

**Keywords:** bismuth oxoiodide; tricobalt tetroxide; persulfate; endocrine-disrupting chemical; mechanism



**Citation:** Zhang, J.; Liu, C.; Lin, Z.; Chen, Q. Heterogeneous Activation of Persulfate by Petal-Shaped  $\text{Co}_3\text{O}_4@\text{BiOI}$  to Degrade Bisphenol AF. *Water* **2024**, *16*, 2887. <https://doi.org/10.3390/w16202887>

Academic Editor: P. V. Nidheesh

Received: 16 August 2024

Revised: 27 September 2024

Accepted: 9 October 2024

Published: 11 October 2024



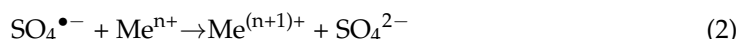
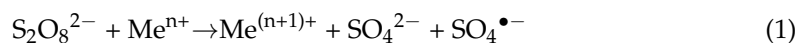
**Copyright:** © 2024 by the authors. Licensee MDPI, Basel, Switzerland. This article is an open access article distributed under the terms and conditions of the Creative Commons Attribution (CC BY) license (<https://creativecommons.org/licenses/by/4.0/>).

## 1. Introduction

Bisphenol A (BPA) is widely used in the synthesis of plastics and resins. However, BPA has been identified as an endocrine-disrupting chemical (EDC), which can severely impair the nervous, immune, and reproductive systems of organisms even at low doses [1]. As the use of BPA has been restricted in several countries, a number of chemicals with similar structures, such as bisphenol AF (BPAF), have been developed as replacements [2,3]. As a result of the large-scale production and widespread application in various industries, concentrations of BPAF up to 15.3  $\mu\text{g}/\text{L}$  have been detected in rivers, groundwater, sewage, and landfill site leachate [4]. Reports have shown that BPAF exhibits a reproductive toxicity and endocrine-disrupting effect equivalent to or even greater than BPA [5]. Moreover, BPAF has a longer half-life and poorer biodegradability [6]. Various methods have been developed to treat BPAF in wastewater, including montmorillonite-mediated photodegradation [7], ferrate oxidation [8], periodate activation [9], catalytic peroxymonosulfate (PMS) oxidation [10], and chlorination [11]. These methods exhibit a number of shortcomings, such as high cost, complicated operation, and secondary pollution, which hinder practical application [12–14]. Consequently, an efficient BPAF treatment and removal method is urgently required.

The application of advanced oxidation processes based on sulfate radicals ( $\text{SO}_4^{\bullet-}$ ) in the degradation of pollutants in water samples is emerging as an effective treatment [15]. There are a number of methods for activating persulfate, including thermal activation [16], ultrasonic activation [17], photoactivation [18], transition metal activation [19], and synergistic activation techniques [20]. Transition metal activation has emerged as a promising oxidation technology that does not require additional energy, operating under mild reaction

conditions to deliver high reaction rates [21,22]. The transition metal ions ( $\text{Fe}^{2+}$ ,  $\text{Cu}^{2+}$ ,  $\text{Mn}^{2+}$ , and  $\text{Co}^{2+}$ ) activate PS by cleaving the O-O bond via electron transfer [23] (Equations (1) and (2)).  $\text{Co}^{2+}$  has been confirmed superior to other transition metal ions in activating PMS/PS, but the discharge of toxic  $\text{Co}^{2+}$  in homogeneous catalytic systems presents serious environmental issues. To overcome the problem of ion dissolution, research has shifted to consider the use of cobalt-based heterogeneous catalysts [24].



Attention has now turned to tricobalt tetroxide ( $\text{Co}_3\text{O}_4$ ) due to the low associated cobalt dissolution and high catalytic activity, though catalytic performance is usually attenuated by particle agglomeration [25]. Increasing contact of free radicals with pollutants is key to improving the efficiency of PS activation by heterogeneous catalysts [26]. Chen et al. prepared BC- $\text{Co}_3\text{O}_4$  to activate PMS for antibiotic degradation by loading  $\text{Co}_3\text{O}_4$  on rice straw-derived biochar. The results have shown that the use of biochar introduces porosity and facilitates the transfer of Oxone to the  $\text{Co}_3\text{O}_4$  active sites with the subsequent generation of free radicals [27]. Su et al. synthesized  $\text{Co}_3\text{O}_4$ /polyurushiol 3D-graphene and  $\text{Co}_3\text{O}_4$ /polyurushiol-graphene/polyurethane foam composite materials with hierarchical porous structures using a simple solvothermal method to catalyze PMS for the degradation of antibiotics. The results have shown that the antibiotic rate can reach 97.8% in only 0.5 min [28].

In this study, a  $\text{Co}_3\text{O}_4$ @BiOI composite material with a petal structure has been prepared using a simple hydrothermal synthesis strategy. The application of  $\text{Co}_3\text{O}_4$ @BiOI combined with PS to remove refractory organics (BPAF) in water is explored for the first time. The morphology, crystal form, components, surface element valence, and chemical bond energy have been analyzed using an array of characterization techniques. The latter includes scanning electron microscopy (SEM), transmission electron microscopy (TEM), X-ray diffraction (XRD), and Fourier-transform infrared spectroscopy (FT-IR). In addition, X-ray photoelectron spectroscopy (XPS), electron paramagnetic resonance (EPR), and quenching tests were conducted to explore the reaction mechanism associated with the  $\text{Co}_3\text{O}_4$ @BiOI/PS system. This work extends the current understanding of BPAF degradation in  $\text{SO}_4^{\bullet-}$ -based advanced oxidation processes.

## 2. Materials and Methods

### 2.1. Chemicals and Reagents

Bisphenol AF ( $\text{C}_{15}\text{H}_{10}\text{F}_6\text{O}_2$ ), bismuth nitrate pentahydrate ( $\text{Bi}(\text{NO}_3)_3 \cdot 5\text{H}_2\text{O}$ ), persulfate (PS) were purchased from Sigma-Aldrich (Shanghai, China). Tricobalt tetraoxide ( $\text{Co}_3\text{O}_4$ ) and potassium iodide (KI) were purchased from Kelong Chemical (Chengdu, China).

### 2.2. Preparation of $\text{Co}_3\text{O}_4$ @BiOI

Different ratios of  $\text{Co}_3\text{O}_4$ @BiOI samples were prepared by a hydrothermal method. The appropriate mass ratios of  $\text{Bi}(\text{NO}_3)_3 \cdot 5\text{H}_2\text{O}$  and  $\text{Co}_3\text{O}_4$  were dissolved in 30 mL absolute ethanol and stirred at 300 rpm for 30 min to obtain solution A. KI (0.4980 g) was dissolved into 30 mL deionized water to obtain solution B. Solution B was slowly added into stirring solution A. The mixed solution was ultrasonicated for 30 min, then the mixed solution was transferred into a stainless 100 mL Teflon-lined autoclave, sealed, and kept at 180 °C for 24 h. The as-prepared samples were washed with deionized water and absolute ethanol several times and then dried at 80 °C in an oven for 24 h.

### 2.3. Catalyst Characterization

An Ultima IV diffractometer (Rigaku, Tokyo, Japan) was employed to analyze the crystal structure of the material, using Cu  $K\alpha$  radiation ( $\lambda = 1.54184 \text{ \AA}$ ), an operating voltage of 40 kV, operating current of 40 mA. Particle structure and morphology, surface

composition, and crystal lattice spacing were determined using a JSM-7500F field emission-SEM (JEOL, Tokyo, Japan) and a high-resolution transmission electron microscope (FEI Talos F200x, Waltham, MA, USA). The electron paramagnetic resonance (EPR) spectra were obtained on a spectrometer (Bruker EMX-PLUS, Karlsruhe, Germany). Surface functional groups were analyzed by Fourier-transform infrared (FT-IR) spectroscopy (Spectrum 1000, PerkinElmer, Waltham, WA, USA).

### 3. Results and Discussion

#### 3.1. Characteristic of $\text{Co}_3\text{O}_4@\text{BiOI}$

The phase and crystallographic structure of the materials were determined by XRD. The XRD patterns of the synthesized  $\text{Co}_3\text{O}_4@\text{BiOI}$  nanomaterial are shown in Figure 1. All diffraction peaks from the  $\text{Co}_3\text{O}_4@\text{BiOI}$  catalyst were in good accordance with the result of JCPDS No.42-1467. The peaks at  $2\theta = 19.00^\circ$ ,  $31.27^\circ$ ,  $36.85^\circ$ ,  $59.35^\circ$ , and  $65.23^\circ$  correspond to the (111), (220), (311), (511), and (440) planes, respectively. The XRD pattern of pure BiOI corresponds to the tetragonal structure and the peaks matched very well with the standard diffraction pattern (JCPDS No.10-0445). The peaks at  $2\theta = 9.66^\circ$ ,  $29.65^\circ$ ,  $31.66^\circ$ ,  $45.38^\circ$ ,  $46.48^\circ$ ,  $55.15^\circ$ ,  $66.12^\circ$ , and  $75.13^\circ$  indexed to the (001), (102), (110), (200), (201), (221), (220), and (310) planes of BiOI microspheres.

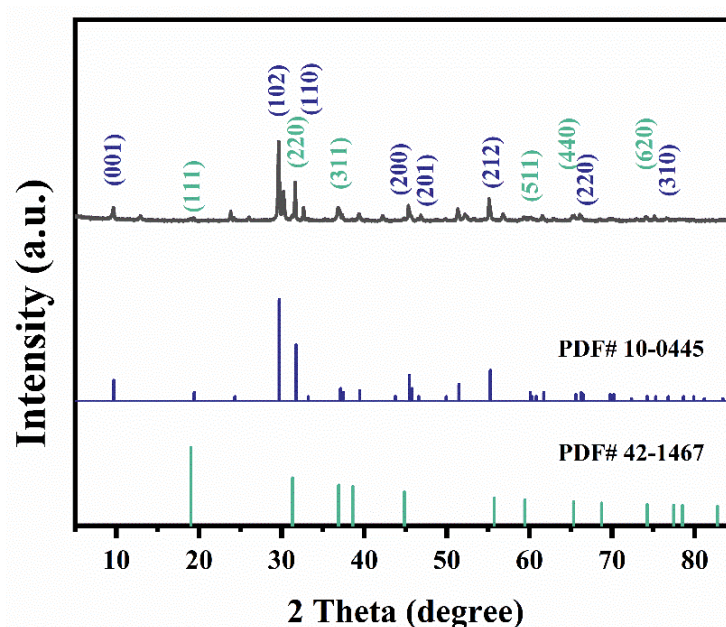
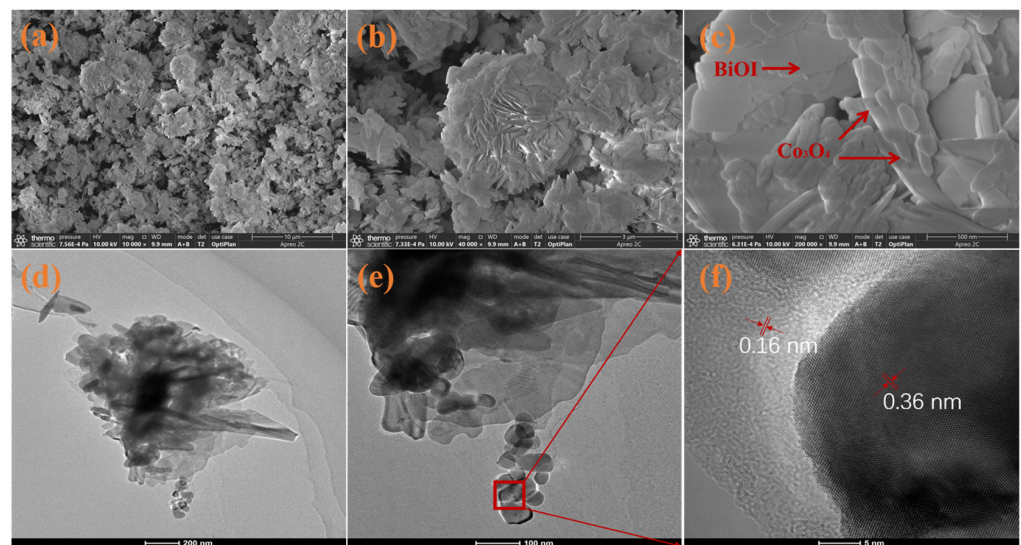


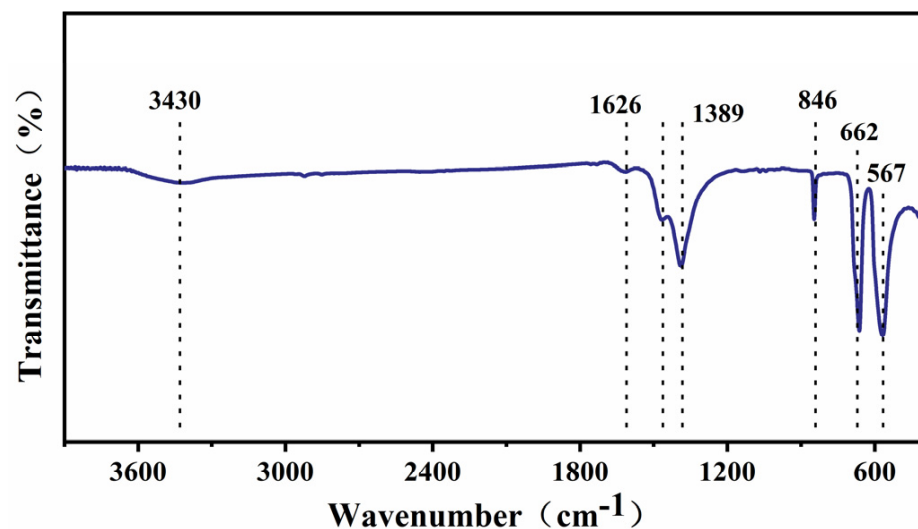
Figure 1. XRD of as-synthesized  $\text{Co}_3\text{O}_4@\text{BiOI}$ .

Figure 2a–c illustrate the morphologies and crystal structures of the prepared  $\text{Co}_3\text{O}_4@\text{BiOI}$ . As shown in Figure 2a, the BiOI [29] nanosheets exhibit a petal-shaped distribution with rod-shaped  $\text{Co}_3\text{O}_4$  particles attached to the nanosheet surface. Further insights into the interior structure of  $\text{Co}_3\text{O}_4@\text{BiOI}$  nanocomposites were obtained by transmission electron microscopy (TEM). Figure 2d–f show the typical TEM image of the  $\text{Co}_3\text{O}_4@\text{BiOI}$  nanocomposites, which has revealed an orderly arrangement of atoms or groups of atoms associated with the material. Application of the Fourier-transform algorithm has identified two crystal lattice spacings in the composite material, where the spacing (0.16 nm) for  $\text{Co}_3\text{O}_4$  is consistent with the reported findings [30,31]. However, the crystal lattice spacing for BiOI (0.36 nm) is higher than the value (0.28 nm) given in the literature [32,33], suggesting that the  $\text{Co}_3\text{O}_4$  and BiOI particles are closely linked together at the nanometer level.



**Figure 2.** SEM (a–c) and TEM (d–f) images of as-synthesized  $\text{Co}_3\text{O}_4@\text{BiOI}$ .

Characterization of the  $\text{Co}_3\text{O}_4@\text{BiOI}$  composite by FTIR generated the spectra presented in Figure 3. Characteristic absorption peaks at  $5,671,375$  and  $1626\text{ cm}^{-1}$  are observed in BiOI [34]. In addition, peaks at  $662$  and  $579\text{ cm}^{-1}$  are attributed to Co–O bond stretching in the  $\text{Co}^{2+}$ -coordinated tetrahedron and the Co–O bond in the  $\text{Co}^{3+}$ -coordinated octahedron, respectively [35].



**Figure 3.** FT–IR spectra of as-synthesized  $\text{Co}_3\text{O}_4@\text{BiOI}$ .

### 3.2. Evaluation of Catalytic Efficiency

#### 3.2.1. Effect of Doping

The effect of different levels of  $\text{Co}_3\text{O}_4$  doping (0.1%  $\text{Co}_3\text{O}_4@\text{BiOI}$ , 0.5%  $\text{Co}_3\text{O}_4@\text{BiOI}$ , 5%  $\text{Co}_3\text{O}_4@\text{BiOI}$ , 10%  $\text{Co}_3\text{O}_4@\text{BiOI}$ , 20%  $\text{Co}_3\text{O}_4@\text{BiOI}$ , and 50%  $\text{Co}_3\text{O}_4@\text{BiOI}$ ) on the catalytic activity was assessed. As shown in Figure 4,  $\text{Co}_3\text{O}_4$  doping had a significant influence on the BPAF removal rate, with the highest activity delivered by 50%  $\text{Co}_3\text{O}_4@\text{BiOI}$ , where the BPAF in water was almost completely removed within 30 min. The 50%  $\text{Co}_3\text{O}_4@\text{BiOI}$  composite was accordingly selected for subsequent testing.

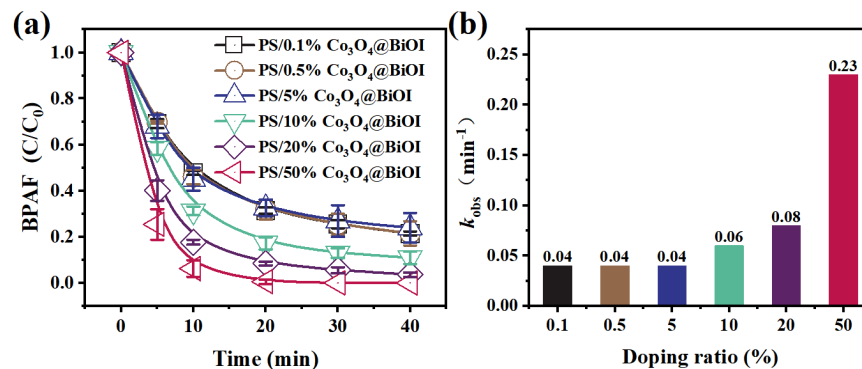


**Figure 4.** Comparison of the Co<sub>3</sub>O<sub>4</sub>@BiOI/PS system. (a) Effect of different Co doping on the degradation; (b) kinetics.

### 3.2.2. Comparison Experiment

In this study, blank control systems (PS, BiOI/PS, Co<sub>3</sub>O<sub>4</sub>/PS, Co<sub>3</sub>O<sub>4</sub>@BiOI, and Co<sub>3</sub>O<sub>4</sub>@BiOI/PS) were employed to assess the catalytic performance of Co<sub>3</sub>O<sub>4</sub>@BiOI. As shown in Figure 5, minor changes were observed in the BPAF removal rate from the aqueous solution with the addition of PS or Co<sub>3</sub>O<sub>4</sub>@BiOI alone. The removal rate by Co<sub>3</sub>O<sub>4</sub>@BiOI/PS was markedly higher than that recorded for BiOI/PS (26.4%) and Co<sub>3</sub>O<sub>4</sub>/PS (9.3%) under the same conditions. The results have established that the Co<sub>3</sub>O<sub>4</sub>@BiOI composite prepared by adding Co<sub>3</sub>O<sub>4</sub>-modified BiOI exhibited significantly higher activity than pure BiOI or Co<sub>3</sub>O<sub>4</sub> before modification.

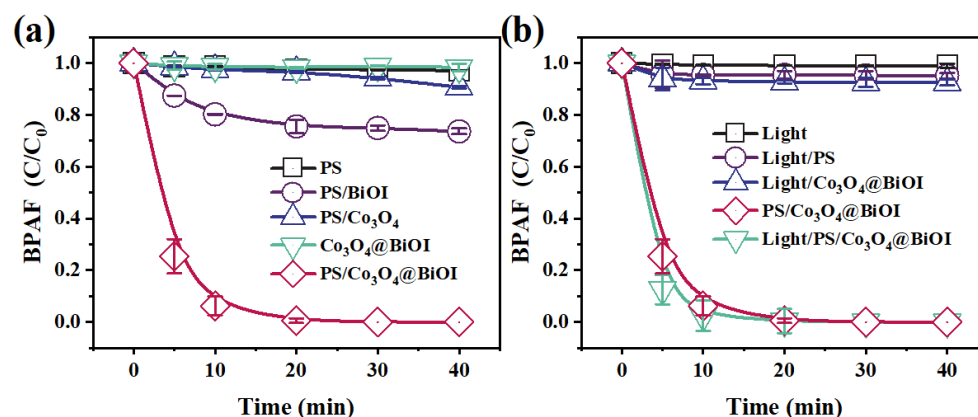


**Figure 5.** (a) A controlled experiment of different systems; (b) control experiment under light/without light system.

Furthermore, the catalytic performance was evaluated using extra light/without extra light control systems (extra light only, extra light/PS, extra light/Co<sub>3</sub>O<sub>4</sub>@BiOI, extra light/Co<sub>3</sub>O<sub>4</sub>@BiOI/PS, and without extra light Co<sub>3</sub>O<sub>4</sub>@BiOI/PS). There was no apparent effect on BPAF removal under the extra light only, extra light/PS, and extra light/Co<sub>3</sub>O<sub>4</sub>@BiOI conditions. In comparing extra light/Co<sub>3</sub>O<sub>4</sub>@BiOI/PS with without extra light Co<sub>3</sub>O<sub>4</sub>@BiOI/PS, the BPAF degradation rate by the extra light/Co<sub>3</sub>O<sub>4</sub>@BiOI/PS system was slightly higher than without extra light Co<sub>3</sub>O<sub>4</sub>@BiOI/PS in the first 10 min of the reaction, but both systems converged with a near-complete degradation of BPAF within 30 min. The reaction system without extra light could save the energy required for light irradiation processing and had greater economic advantages, so the subsequent experiments were conducted under conditions without extra light.

### 3.2.3. Effect of PS Concentration

The effects of the PS dosage on the BPAF removal rate by Co<sub>3</sub>O<sub>4</sub>@BiOI/PS have been examined. As shown in Figure 6, the degradation rate was 1.7% in the absence of PS,

indicating negligible catalytic activity or BPAF adsorption on the composite. Increasing the PS dosage from 0.05 mM to 0.1 mM resulted in an increase in the BPAF degradation rate from 86.9% to 95.2%, and the  $k_{\text{obs}}$  value was raised from  $0.050 \text{ min}^{-1}$  to  $0.075 \text{ min}^{-1}$ . The degradation was largely invariant with a PS dosage increase to 0.2 mM, 0.4 mM, and 0.8 mM generating values of 95.3%, 96.5%, and 96.7%, with associated  $k_{\text{obs}}$  of  $0.077 \text{ min}^{-1}$ ,  $0.082 \text{ min}^{-1}$ , and  $0.083 \text{ min}^{-1}$ , respectively, demonstrating a stable BPAF oxidation rate. In further tests, the PS dosage was fixed at 0.1 mM.

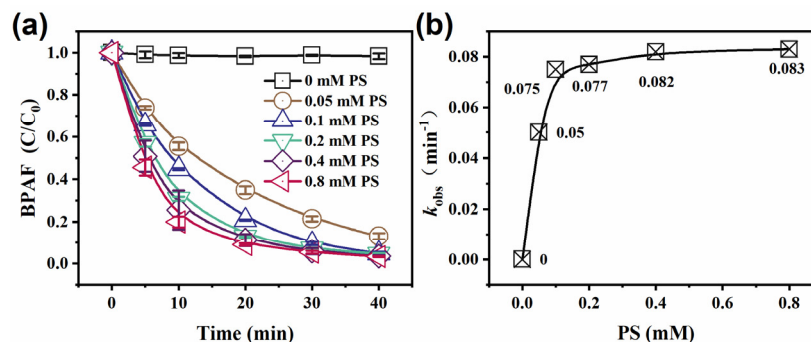


**Figure 6.** Effect of PS dosage on BPAF removal in the  $\text{Co}_3\text{O}_4\text{@BiOI/PS}$  system. (a) BPAF removal; (b)  $k_{\text{obs}}$  of BPAF.

### 3.2.4. Effect of Initial pH

The influence of the initial pH on the degradation of BPAF by  $\text{Co}_3\text{O}_4\text{@BiOI/PS}$  is shown in Figure 7. The removal rate was lowest at pH 3.0 with higher values as the pH was increased to 5.0, 9.0, and pH 11.0. The degradation rate and  $k_{\text{obs}}$  remained at low levels in neutral or acid solution. Under strongly acidic (pH 3.0) conditions, the system produces more protons that consume the  $\bullet\text{O}_2^-$  generated. The acid conditions can inhibit the production of other reactive groups, limiting the degradation of BPAF [36]. At an initial pH of 9.0, the BPAF degradation rate was 70.6%, lower than that (95.2%) at an initial pH of 7.85. An increase in the initial pH to 11.0 resulted in the near-complete degradation of BPAF (99.5%), with a  $k_{\text{obs}}$  of  $0.126 \text{ min}^{-1}$ . The increase in  $\text{OH}^-$  under strongly alkaline conditions results in an increased  $\bullet\text{OH}$  concentration in the system, enhancing the degradation rate of BPAF. The results demonstrate that  $\text{Co}_3\text{O}_4\text{@BiOI/PS}$  is sensitive to the initial solution pH and works more effectively in strongly alkaline environments.

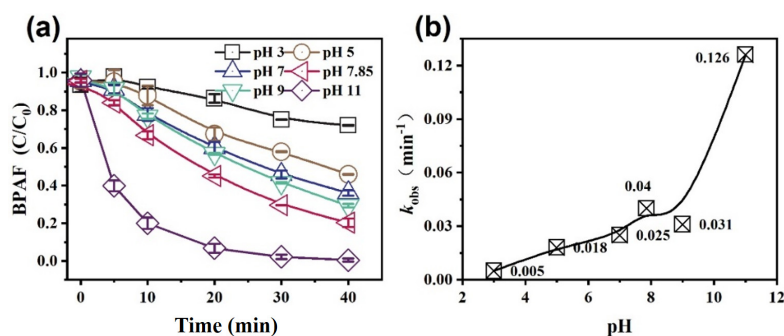


**Figure 7.** Effect of the solution pH on BPAF removal in the  $\text{Co}_3\text{O}_4\text{@BiOI/PS}$  system. (a) BPAF removal; (b)  $k_{\text{obs}}$  of BPAF (experimental conditions:  $[\text{Co}_3\text{O}_4\text{@BiOI}]_0 = 150 \text{ mg/L}$ ,  $[\text{PS}]_0 = 0.1 \text{ mM}$ ,  $[\text{BPAF}]_0 = 5 \text{ mg/L}$ , initial pH = 3.0–11.0,  $T = 25 \pm 1 \text{ }^\circ\text{C}$ , reaction time: 40 min).

### 3.2.5. Effect of Inorganic Anions

The effects of common inorganic anions (bicarbonate ( $\text{HCO}_3^-$ ), chloride ( $\text{Cl}^-$ ), sulfate ( $\text{SO}_4^{2-}$ ), and nitrate ( $\text{NO}_3^-$ ) ions) in water on the degradation of BPAF by  $\text{Co}_3\text{O}_4\text{@BiOI/PS}$  have been examined as an important consideration in terms of practical application.

As shown in Figure 8a, the degradation rate exhibited a two-way trend of increasing and decreasing values in the case of the  $\text{HCO}_3^-$  concentration in the solution. The degradation rate was 100%, 95.0%, and 47.6% at 10 mM, 50 mM, and 100 mM  $\text{HCO}_3^-$ , respectively. This suggests an optimum concentration of  $\text{HCO}_3^-$  in terms of BPAF oxidative degradation where the reaction system is suppressed at high concentrations. Relevant studies have revealed that a low concentration of  $\text{HCO}_3^-$  can serve to quench  $\text{SO}_4^{\bullet-}$  and  $\bullet\text{OH}$ , producing the bicarbonate radical ( $\text{HCO}_3^{\bullet-}$ ) with low associated activity in the oxidative degradation of organic pollutants, resulting in a lower BPAF conversion [37,38].

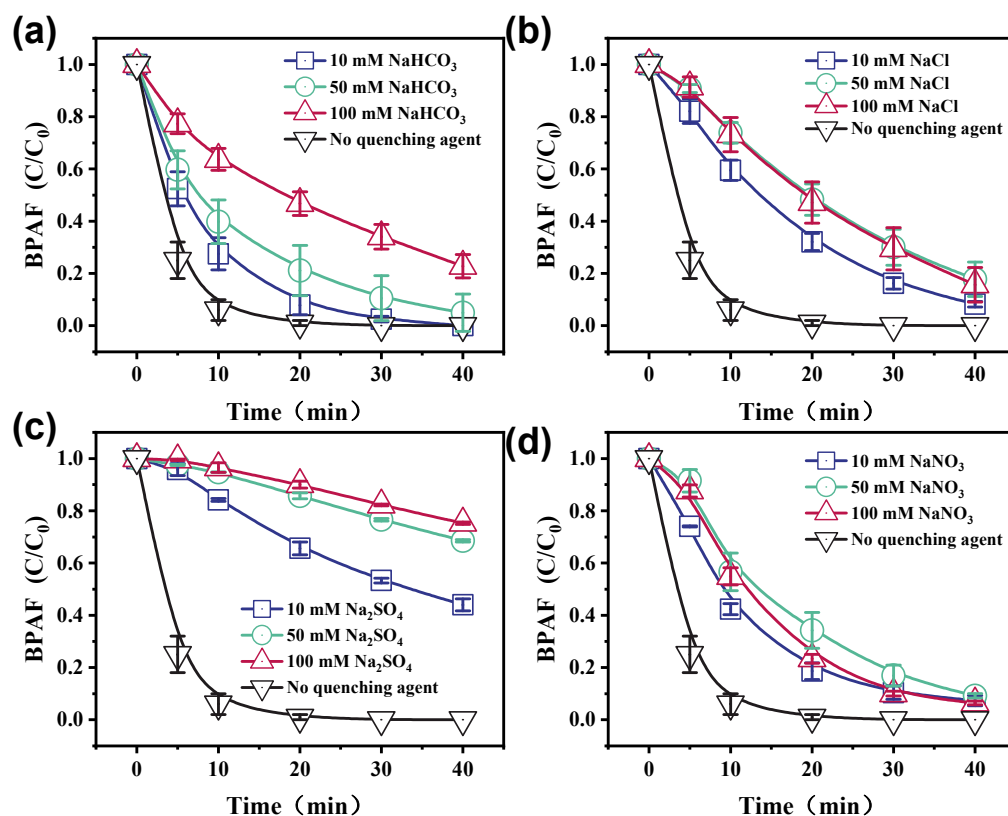


**Figure 8.** Effects of anions at different concentrations on BPAF removal in the  $\text{Co}_3\text{O}_4@\text{BiOI}/\text{PS}$  system. (a)  $\text{HCO}_3^-$ , (b)  $\text{Cl}^-$ , (c)  $\text{SO}_4^{2-}$ , (d)  $\text{NO}_3^-$ . (Experimental conditions:  $[\text{Co}_3\text{O}_4@\text{BiOI}]_0 = 150 \text{ mg/L}$ ,  $[\text{PS}]_0 = 0.1 \text{ mM}$ ,  $[\text{BPAF}]_0 = 5 \text{ mg/L}$ , initial pH = 3.0–11.0,  $T = 25 \pm 1 \text{ }^\circ\text{C}$ , reaction time: 40 min).

The results presented in Figure 8b,c show the dependence of BPAF degradation on the  $\text{Cl}^-$  and  $\text{SO}_4^{2-}$  concentrations, which served to inhibit the reactivity of  $\text{Co}_3\text{O}_4@\text{BiOI}/\text{PS}$ . As can be seen in Figure 8b, the BPAF degradation rate was lowered from 100% to 91.8%, 84.4%, and 82.2%, respectively, following the addition of 10 mM, 50 mM, and 100 mM  $\text{Cl}^-$  to the solution under the controlled experimental conditions. The  $\text{Cl}^-$  in the system can react with  $\text{SO}_4^{\bullet-}$  to generate  $\text{Cl}\bullet$  and  $\text{Cl}_2^{\bullet-}$  with low oxidation capability, impeding BPAF degradation [39]. Moreover, the degradation rate of BPAF dropped to 56.0%, 31.5%, and 24.7%, respectively, after adding 10 mM, 50 mM, and 100 mM  $\text{SO}_4^{2-}$  (Figure 8c), demonstrating inhibition by  $\text{SO}_4^{2-}$  that was more pronounced at higher concentrations.

The inclusion of varying  $\text{NO}_3^-$  concentrations had a minor effect on BPAF degradation (Figure 8d), resulting in a slight increase from 92.7% to 90.8% and 93.6% at 10 mM, 50 mM, and 100 mM  $\text{NO}_3^-$ , respectively.

### 3.3. Reusability of $\text{Co}_3\text{O}_4@\text{BiOI}$

Continuous and intermittent cyclic recycling experiments were conducted to assess the stability and reusability of the  $\text{Co}_3\text{O}_4@\text{BiOI}$  composite. The experimental results shown

in Figure 9 reveal that after two continuous cyclic degradation experiments, BPAF removal was still close to 100%, demonstrating catalyst stability. The cyclic BPAF degradation was continued with catalyst recycles, and the level of degradation declined from 91% to 84% and 81% over the third to fifth recycle. The intermediates produced during oxidative degradation in repeated reactions can poison the catalyst and lower the activity. When compared with similar catalytic materials, the  $\text{Co}_3\text{O}_4@\text{BiOI}$  composite exhibited good stability. Dissolution of  $\text{Co}^{2+}$  was established where the concentration of cobalt ions in the solution (0.07 mg/L) at the end of the reaction. The results demonstrate that the  $\text{Co}_3\text{O}_4@\text{BiOI}$  catalyst has good reusability and a low metal dissolution rate with no serious environmental pollution impact, suggesting viable practical application.

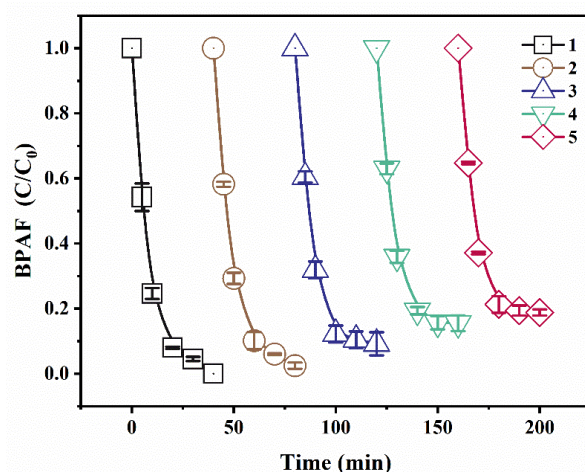


Figure 9. Recycling test on the  $\text{Co}_3\text{O}_4@\text{BiOI}/\text{PS}$  system.

Figure 10 graphically represents the XRD results before and after the reaction. Assessment of Figure 10 reveals that the  $\text{Co}_3\text{O}_4@\text{BiOI}$  composite's XRD peaks, following the reaction, vanished at  $2\theta$  values of  $9.66^\circ$ ,  $55.15^\circ$ ,  $75.13^\circ$ ,  $31.27^\circ$ ,  $59.35^\circ$ , and  $64.10^\circ$  when juxtaposed with its pre-reaction state. The lattice planes of BiOI at (001), (212), and (310) correspond with the XRD peaks at  $2\theta$  of  $9.66^\circ$ ,  $55.15^\circ$ , and  $75.13^\circ$  whilst the  $\text{Co}_3\text{O}_4$  lattice planes at (220), (511), and (620) consistently align with the XRD peaks at  $2\theta$  of  $31.27^\circ$ ,  $59.35^\circ$ , and  $64.10^\circ$ . This strengthens the argument that the  $\text{Co}_3\text{O}_4$  and BiOI constituents in the  $\text{Co}_3\text{O}_4@\text{BiOI}$  composite are participants in the oxidation process.

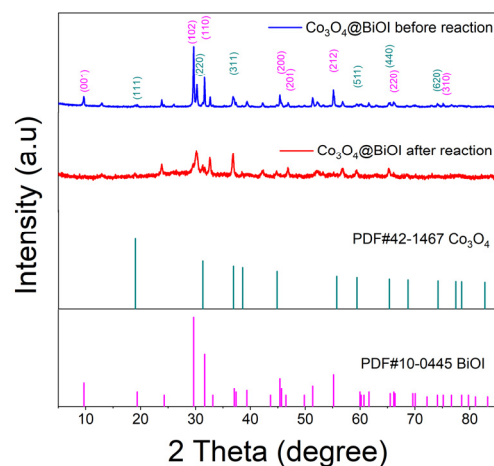
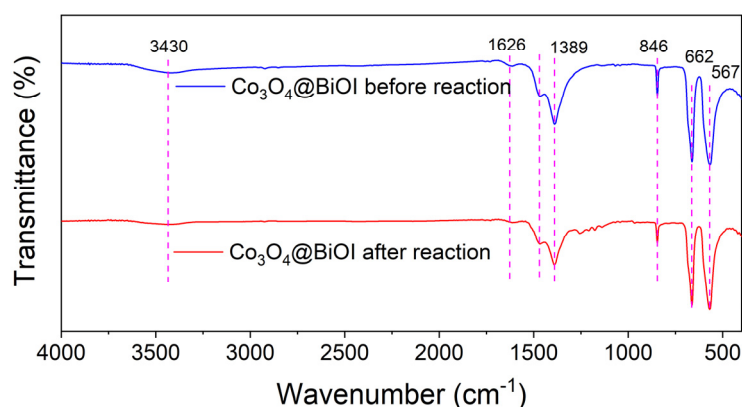


Figure 10. XRD patterns of the synthesized  $\text{Co}_3\text{O}_4@\text{BiOI}$  before and after reaction. (Experimental conditions: initial  $[\text{Co}_3\text{O}_4@\text{BiOI}]_0 = 150 \text{ mg/L}$ ,  $[\text{PS}]_0 = 0.1 \text{ mM}$ ,  $[\text{BPAF}]_0 = 5 \text{ mg/L}$ , initial  $\text{pH} = 7.85 \pm 0.2$ ,  $T = 25 \pm 1 \text{ }^\circ\text{C}$ ).



Figure 11 demonstrates a negligible modification in the FT-IR spectra of the  $\text{Co}_3\text{O}_4\text{@BiOI}$  composite before and after the reaction, indicating the high stability of the  $\text{Co}_3\text{O}_4\text{@BiOI}$  chemical bonds.



**Figure 11.** FT-IR patterns of the synthesized  $\text{Co}_3\text{O}_4\text{@BiOI}$  before and after reaction. (Experimental conditions: initial  $[\text{Co}_3\text{O}_4\text{@BiOI}]_0 = 150 \text{ mg/L}$ ,  $[\text{PS}]_0 = 0.1 \text{ mM}$ ,  $[\text{BPAF}]_0 = 5 \text{ mg/L}$ , initial  $\text{pH} = 7.85 \pm 0.2$ ,  $T = 25 \pm 1 \text{ }^\circ\text{C}$ ).

### 3.4. PS Activation Mechanism of $\text{Co}_3\text{O}_4\text{@BiOI}$

#### 3.4.1. Identification of Active Species

Methanol (MeOH), tert-butyl alcohol (TBA), L-histidine, and p-benzoquinone (BQ) can act as quenchers of  $\text{SO}_4^{\bullet-}$ ,  $\bullet\text{OH}$ ,  $\text{O}_2^{\bullet-}$ , and  $^1\text{O}_2$ , respectively, and were used to identify the major active species produced in the PS oxidation reaction system. As shown in Figure 12a,b, the removal rate of BPAF fell from 95.8% to 53.2%, 21.1%, and 14.4%, respectively, after adding 10 mM, 50 mM, and 100 mM MeOH to the  $\text{Co}_3\text{O}_4\text{@BiOI/PS}$  system. This response indicates that both  $\text{SO}_4^{\bullet-}$  and  $\bullet\text{OH}$  may play a crucial role in the oxidative degradation of BPAF. The removal rate of BPAF was decreased to 93.2%, 45.8%, and 10%, respectively, with the addition of increasing concentrations (10 mM, 50 mM, and 100 mM) of TBA. The inhibition caused by 100 mM TBA was equivalent to that recorded for 100 mM MeOH, suggesting that  $\bullet\text{OH}$  plays a leading role in the reaction system. The inhibition due to a low concentration of TBA was less than that observed with MeOH, suggesting the crucial role of  $\bullet\text{OH}$  in degradation though  $\text{SO}_4^{\bullet-}$  and  $\bullet\text{OH}$  are produced simultaneously in the reaction system. The removal rate of BPAF decreased to 87.3%, 21.6%, and 12.2%, respectively, after adding 1 mM, 5 mM, and 10 mM L-histidine (Figure 12c), suggesting the possible presence of  $^1\text{O}_2$  in the  $\text{Co}_3\text{O}_4\text{@BiOI/PS}$  system. Moreover, the removal rate of BPAF only dropped to 93.4%, 88.6%, and 75.7% after adding 0.1 mM, 0.5 mM, and 1 mM BQ, suggesting the possible presence of  $\text{O}_2^{\bullet-}$  in the  $\text{Co}_3\text{O}_4\text{@BiOI/PS}$  system but its contribution to the oxidative degradation of BPAF is relatively weak.

The results of the quenching tests using the chemical probe method have revealed that four active species ( $\text{SO}_4^{\bullet-}$ ,  $\bullet\text{OH}$ ,  $\text{O}_2^{\bullet-}$ , and  $^1\text{O}_2$ ) may be formed in the  $\text{Co}_3\text{O}_4\text{@BiOI/PS}$  system. We have employed EPR spectroscopy to further determine the free and non-free radicals found in the system. In the tests, 5,5-dimethyl-1-pyrroline N-oxide (DMPO) served as a free radical scavenger for  $\text{SO}_4^{\bullet-}$ ,  $\bullet\text{OH}$ , and  $\text{O}_2^{\bullet-}$ , and 2,2,6,6-tetramethylpiperidine-1-oxyl (TEMP) was used as a non-free radical scavenger for  $^1\text{O}_2$ . As shown in Figure 13a, a clear signal with four split lines at an intensity ratio of 1:2:2:1 for the DMPO-OH adduct and a relatively weak signal with six split lines at an intensity ratio of 1:1:1:1:1:1 for the DMPO- $\text{SO}_4$  adduct were observed at 3 min after adding DMPO to the system. The signal for the DMPO- $\text{SO}_4$  adduct was weaker than the DMPO-OH adduct. This is attributed to the rapid conversion of  $\text{SO}_4^{\bullet-}$  produced in the reaction system to  $\bullet\text{OH}$  or conversion of the DMPO- $\text{SO}_4$  adduct into DMPO-OH adduct. The signals for DMPO- $\text{SO}_4$  and DMPO-OH adducts were gradually enhanced over the reaction time, consistent with the continuous

production and gradual increase in  $\text{SO}_4^{\bullet-}$  and  $\bullet\text{OH}$  in the system over the first 15 min of the reaction.

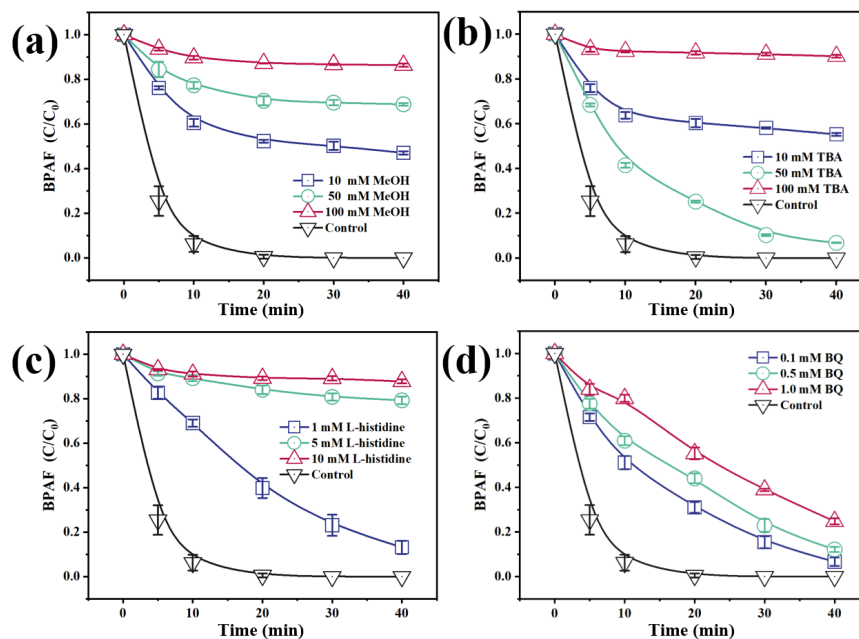


**Figure 12.** Quenching tests for different reactive oxygen species ( $[\text{Co}_3\text{O}_4@\text{BiOI}]_0 = 150 \text{ mg/L}$ ,  $[\text{PS}]_0 = 0.1 \text{ mM}$ ,  $[\text{BPAF}]_0 = 5 \text{ mg/L}$ , initial  $\text{pH} = 7.85 \pm 0.2$ ,  $T = 25 \pm 1 \text{ }^\circ\text{C}$ ). (a) MeOH; (b) TBA; (c) L-histidine; (d) BQ.

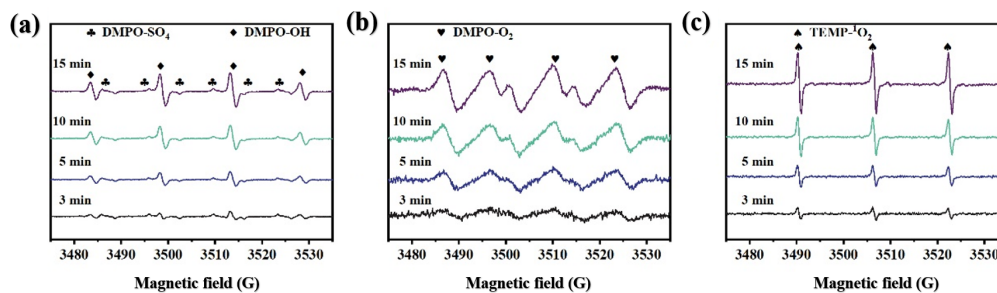


**Figure 13.** The detection results of (a)  $\text{SO}_4^{\bullet-}$ ,  $\bullet\text{OH}$ , (b)  $\bullet\text{O}_2^-$ , and (c)  $^1\text{O}_2$  by EPR technology.

A significant quadruple-peak signal (DMPO- $\text{O}_2$ ) with an intensity ratio of 1:1:1:1 (Figure 13b) was detected by EPR at 3 min after adding DMPO to the system, which is attributed to  $\bullet\text{O}_2^-$ . The intensity of the DMPO- $\text{O}_2$  signal gradually increased as the reaction proceeded. The results indicate that  $\bullet\text{O}_2^-$  is present in the reaction system and increases over the first 15 min of the reaction, which differs from the results of the quenching tests. This may suggest that  $\text{O}_2^{\bullet-}$  mainly serves as an intermediate in the activation of PS by  $\text{Co}_3\text{O}_4@\text{BiOI}$  and is not directly involved in the oxidative degradation of BPAF.

As shown in Figure 13c, a clear triple-peak signal (TEMP- $^1\text{O}_2$ ) with an intensity ratio of 1:1:1 was detected by EPR at 3 min after adding TEMP to the system, proving the presence of  $^1\text{O}_2$  in the system. The TEMP- $^1\text{O}_2$  signal intensity increased over the first 15 min of the reaction, indicating an increased production of  $^1\text{O}_2$  in the system.

In summary, the results confirm the co-existence of free radicals ( $\text{SO}_4^{\bullet-}$ ,  $\bullet\text{OH}$ , and  $\text{O}_2^{\bullet-}$ ) and non-free radicals ( $^1\text{O}_2$ ) in the  $\text{Co}_3\text{O}_4@\text{BiOI}/\text{PS}$  system, which act to synergistically promote the degradation of BPAF in water. The  $\text{O}_2^{\bullet-}$  radical mainly acts as an intermediate to facilitate catalytic oxidation during the activation of PS by  $\text{Co}_3\text{O}_4@\text{BiOI}$ .

### 3.4.2. Catalysis Mechanism

The chemical states and composition of  $\text{Co}_3\text{O}_4@\text{BiOI}$  were characterized by XPS. The XPS survey spectra revealed no variations in the major element species associated with  $\text{Co}_3\text{O}_4@\text{BiOI}$  before and after the reaction, identifying Bi, I, Co, O, and C as the major components. The peaks at 163.6 eV and 158.3 eV in the high-resolution XPS spectra are shown in Figure 14.

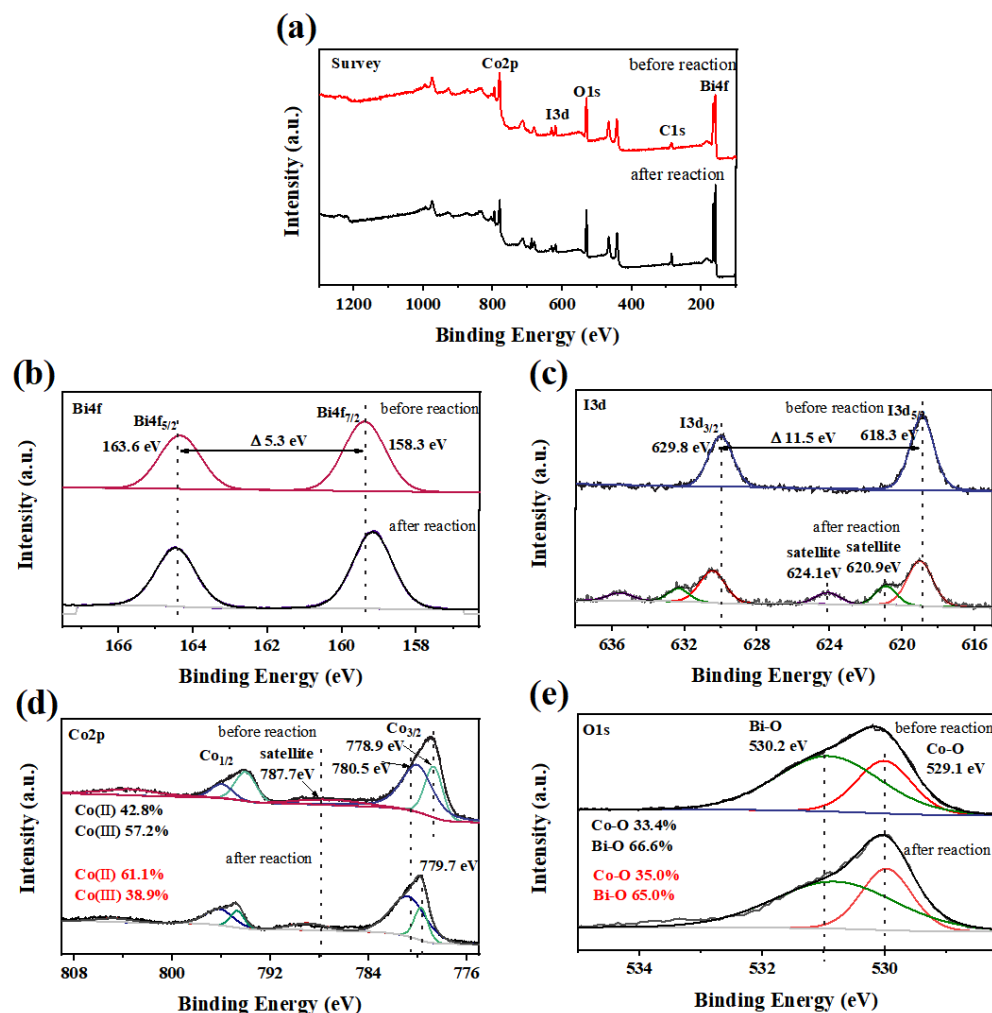
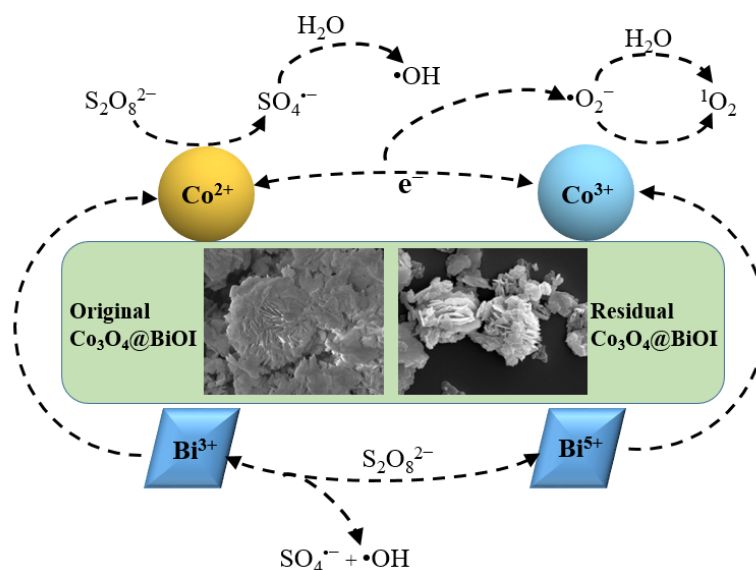


**Figure 14.** XPS spectra of the synthesized  $\text{Co}_3\text{O}_4@\text{BiOI}$ . (a) Survey spectra; (b) Bi 4f; (c) I 3d; (d) Co 2p; (e) O 1s.

Possible changes to the surface chemistry of  $\text{Co}_3\text{O}_4@\text{BiOI}$  in activating PS were assessed by XPS analysis of the composite before and after the reaction (Figure 14). The XPS survey spectra revealed no variations in the major element species associated with  $\text{Co}_3\text{O}_4@\text{BiOI}$  before and after the reaction, identifying Bi, I, Co, O, and C as the major components. As shown in Figure 14b,c, there is no evident alteration in the spectra of Bi 4f and I 3d following the reaction. The XPS analysis has not detected a conversion between Bi(III) and Bi(V) during the reaction. In contrast, the spectra of Co 2p before and after BPAF degradation establish a difference in the Co(II) and Co(III) composition (Figure 14d). The atomic composition of Co(II) and Co(III) was changed from 61.1% and 38.9% to 42.8% and 57.3% after the reaction. This response may be attributed to electron donation by Co(II), increasing the Co(III) content as part of the Co(II)-Co(III)-Co(II) cycle during the catalytic reaction [40]. The results suggest the interactive conversion of Co(II) to Co(III) in the  $\text{Co}_3\text{O}_4@\text{BiOI}$  that promotes PS activation. The spectra of  $\text{O}1s$  before and after the reaction are presented in Figure 14e and show an increase in the relative contribution of Co-O from

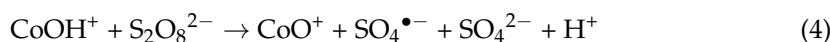
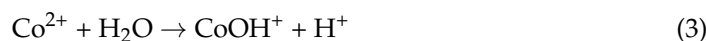
33.4% to 35.0% following the reaction. Moreover, the relative contribution of Bi-O fell from 66.6% to 65.0%, implying that the two types of oxygen were mutually transformed and participated in the oxidation process [8,41].

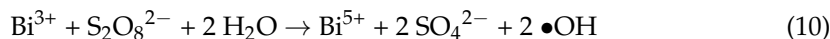
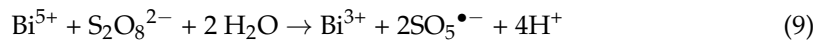
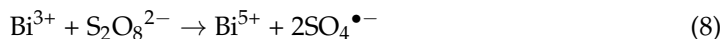
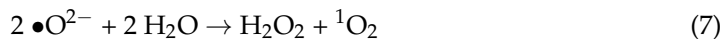
Based on the results of the quenching tests, EPR analysis, and structural changes determined by XPS, a reaction mechanism is proposed that accounts for the activation of PS by  $\text{Co}_3\text{O}_4@\text{BiOI}$ , outlined in Figure 15 and Equations (3)–(10). The combination of the lower-valence Co(II) with the dissociation and adsorption of water produced  $\text{CoOH}^+$  (Equation (3)) on the surface of  $\text{Co}_3\text{O}_4@\text{BiOI}$  and subsequently interacted with PS in solution through hydrogen bond formation [42–44]. Co(II) immediately loses electrons and is oxidized to high-valence Co(III) [42]. O-H and O-O bonds break while accepting electrons to generate highly reactive  $\text{SO}_4^{\bullet-}$  that reacts with water to produce  $\bullet\text{OH}$  (Equations (4) and (5)) [45,46]. The  $\text{CoO}^+$  that is formed (Equation (4)) can react with PS to generate Co(II) and  $\bullet\text{O}^{2-}$  (Equation (6)). The transformation between Co(II) and Co(III) effectively promotes the catalytic activation of PS. Reports in the literature have shown that the redox couple (Bi(III) and Bi(V)) in BiOI can also activate PS and produce free  $\text{SO}_4^{\bullet-}$  and  $\bullet\text{OH}$  (Equations (8)–(10)) [31,38]. We propose that Co(II)/Co(III) and Bi(III)/Bi(V) serve as redox couples that participate in activating PS in the  $\text{Co}_3\text{O}_4@\text{BiOI}/\text{PS}$  system. The two components ( $\text{Co}_3\text{O}_4$  and BiOI) from the  $\text{Co}_3\text{O}_4@\text{BiOI}$  exhibit a synergism that promotes the rapid oxidative degradation of BPAF in water. The XPS analysis has suggested a mutual conversion between lattice oxygen associated with Co-O and Bi-O on the composite surface that contributes to the oxidation process, where  $\bullet\text{O}^{2-}$  generated by  $\text{CoO}^+$  (Equation (6)) reacts with  $\bullet\text{OH}$  in the solution to produce  $^1\text{O}_2$  (Equation (7)), accelerating BPAF removal [47]. In this process,  $\bullet\text{O}^{2-}$  mainly serves as an intermediate in a mass transfer step that promotes catalytic oxidation.



**Figure 15.** The possible mechanisms of BPAF degradation in the  $\text{Co}_3\text{O}_4@\text{BiOI}/\text{PS}$  system.

The Co(II)/Co(III) and Bi(III)/Bi(V) redox couples combine in a synergism that promotes the activation of PS. In addition, surface lattice oxygen plays a key role in BPAF removal. The major active species ( $\text{SO}_4^{\bullet-}$ ,  $\bullet\text{OH}$ ,  $\text{O}_2^{\bullet-}$  and  $^1\text{O}_2$ ) generated during the reaction play synchronous and synergistic roles in converting BPAF to small molecules. The  $\text{SO}_4^{\bullet-}$ ,  $\bullet\text{OH}$ , and  $\text{O}_2^{\bullet-}$  contribute directly to the oxidation process, while  $^1\text{O}_2$  serves as an intermediate in a mass transfer that facilitates catalytic oxidation.





### 3.5. The Proposed Mechanism in $\text{Co}_3\text{O}_4\text{/BiOI}$

We have employed LC-MS analysis to determine the main reaction intermediates and elucidate the BPAF degradation pathway. The TOC concentration in the solution after the reaction was tested to be 1.70 mg/L, and the ratio of mineralization is 66%. A total of 14 intermediates were detected (Table 1). Based on the product distribution and literature reports, three major degradation pathways are proposed, as illustrated in Figure 16. The electron-rich component (benzene ring or p-hydroxyl) of BPAF is attacked by sulfate and hydroxyl generated by PS. The BPAF molecules are converted to phenoxy radicals or the resonance form R1, resulting from a delocalization of unpaired electrons. The  $\beta$ -bonds of benzene rings with a high electron density in the para-position are broken, forming unstable positively charged ions and electronically charged phenol radicals, which are further converted to hydroquinone intermediates (P2 and P3) by hydroxylation and then generate hydroquinone (P4) [39]. The hydroxylated product of BPAF (P5) can undergo ring opening to form P6, a carboxylic acid intermediate, which is converted to P7 by decarbonylation and oxidation and further ring opening and cracking to small molecular products [31]. Hydroxylation of P8 by  $\bullet\text{OH}$ , a monohydroxylated product of BPAF, generates dihydroxylated P10. In addition, P8 may form P9 by ring opening. The presence of two or more adjacent hydroxyl groups can activate polyhydroxylated products, which are prone to oxidation and formation of quinone intermediates that are converted to P6 by ring opening.

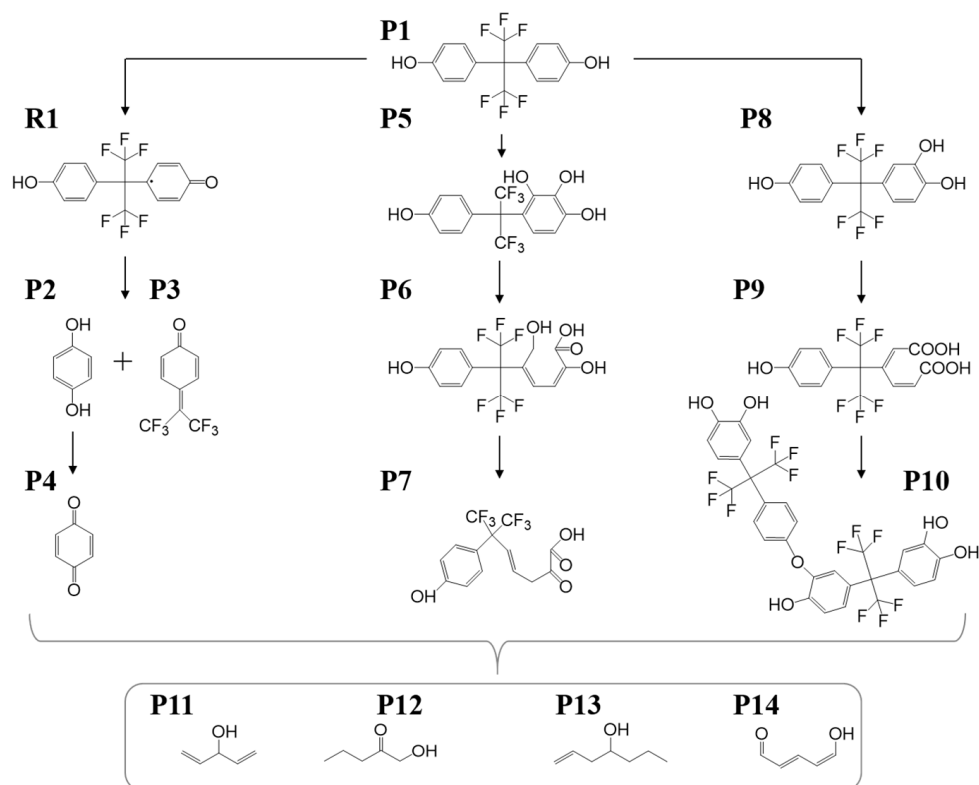


**Figure 16.** Possible degradation pathways of BPAF in the  $\text{Co}_3\text{O}_4\text{/BiOI/PS}$  system.

**Table 1.** Mass and structures of BPAF and its transformation products by the  $\text{Co}_3\text{O}_4@\text{BiOI}/\text{PS}$  system.

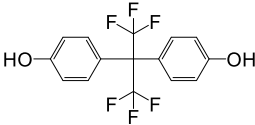
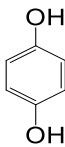
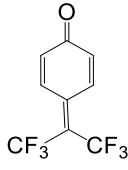
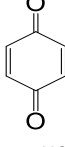
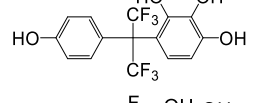
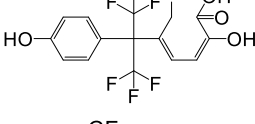
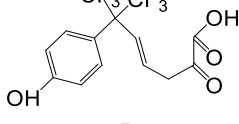
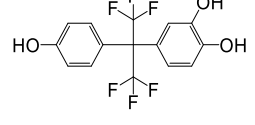
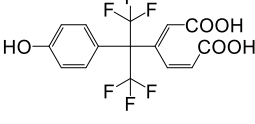
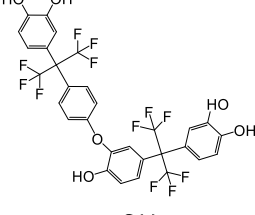
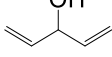
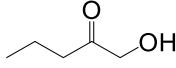
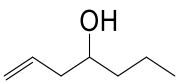
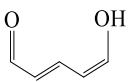
Product ID	M/Z	Formula	Structure
P1	336	$\text{C}_{15}\text{H}_{10}\text{F}_6\text{O}_2$	
P2	110	$\text{C}_6\text{H}_6\text{O}_2$	
P3	242	$\text{C}_{15}\text{H}_{12}\text{F}_4\text{O}_4$	
P4	108	$\text{C}_6\text{H}_4\text{O}_2$	
P5	367	$\text{C}_{15}\text{H}_{10}\text{F}_6\text{O}_4$	
P6	386	$\text{C}_{15}\text{H}_{12}\text{F}_6\text{O}_5$	
P7	356	$\text{C}_6\text{H}_6\text{O}$	
P8	352	$\text{C}_{15}\text{H}_{10}\text{F}_6\text{O}_3$	
P9	384	$\text{C}_{15}\text{H}_{10}\text{F}_6\text{O}_5$	
P10	702	$\text{C}_{30}\text{H}_{18}\text{F}_{12}\text{O}_6$	
P11	84	$\text{C}_5\text{H}_8\text{O}$	
P12	102	$\text{C}_5\text{H}_{10}\text{O}$	

Table 1. Cont.

Product ID	M/Z	Formula	Structure
P13	114	C <sub>7</sub> H <sub>14</sub> O	
P14	98	C <sub>5</sub> H <sub>6</sub> O <sub>2</sub>	

#### 4. Conclusions

In this study, a Co<sub>3</sub>O<sub>4</sub>@BiOI composite catalyst was synthesized and used to promote the efficient degradation of BPAF by activating PS. The experimental results have demonstrated a near-complete removal of BPAF within 30 min at a PS dosage of 0.1 mM. BPAF degradation was suppressed under acidic conditions, promoted with the addition of a particular concentration of HCO<sub>3</sub><sup>−</sup> but impeded by Cl<sup>−</sup>, SO<sub>4</sub><sup>2−</sup>, and high concentrations of HCO<sub>3</sub><sup>−</sup>. Moreover, NO<sub>3</sub><sup>−</sup> had a negligible effect on BPAF degradation. A mechanistic analysis has revealed the co-existence of Co(II)/Co(III) and Bi(III)/Bi(V) redox couples that serve to activate PS, involving synergism between the Co<sub>3</sub>O<sub>4</sub> and BiOI components of the composite that facilitate the oxidative degradation of BPAF in water. Three possible BPAF degradation pathways have been identified for the Co<sub>3</sub>O<sub>4</sub>@BiOI/PS system.

**Author Contributions:** Conceptualization, J.Z. and C.L.; methodology, J.Z.; formal analysis, C.L. and Z.L.; investigation, C.L. and Z.L.; resources, J.Z.; data curation, J.Z. and C.L.; writing—original draft preparation, J.Z. and C.L.; writing—review and editing, J.Z. and C.L.; supervision, Q.C.; project administration, J.Z.; funding acquisition, J.Z. All authors have read and agreed to the published version of the manuscript.

**Funding:** This research was supported by the Chengdu Municipal Science and Technology Bureau (2018-YF09-00041-SN) and Power Construction Corporation of China (DJ-ZDXM-2017-30).

**Data Availability Statement:** Data are available upon request from the corresponding author.

**Conflicts of Interest:** All Authors were employed by the company Chengdu Engineering Corporation Ltd., Power China. The Authors Changling Liu have another Affiliations is the State Key Laboratory of Hydraulics and Mountain River Engineering, Sichuan University. All Authors declare that the research was conducted in the absence of any commercial or financial relationships that could be construed as a potential conflict of interest.

#### References

- Liu, Y.; Lin, Y.; Yen, C.; Miaw, C.; Chen, T.; Wu, M.; Hsieh, C. Identification, contribution, and estrogenic activity of potential EDCs in a river receiving concentrated livestock effluent in Southern Taiwan. *Sci. Total Environ.* **2018**, *636*, 464–476. [[CrossRef](#)] [[PubMed](#)]
- Cimmino, I.; Fiory, F.; Perruolo, G.; Miele, C.; Beguinot, F.; Formisano, P.; Oriente, F. Potential Mechanisms of Bisphenol A (BPA) Contributing to Human Disease. *Int. J. Mol. Sci.* **2020**, *21*, 5761. [[CrossRef](#)] [[PubMed](#)]
- den Braver-Sewradj, S.P.; van Spronsen, R.; Hessel, E.V.S. Substitution of bisphenol A: A review of the carcinogenicity, reproductive toxicity, and endocrine disruption potential of alternative substances. *Crit. Rev. Toxicol.* **2020**, *50*, 128–147. [[CrossRef](#)] [[PubMed](#)]
- Song, S.; Ruan, T.; Wang, T.; Liu, R.; Jiang, G. Distribution and Preliminary Exposure Assessment of Bisphenol AF (BPAF) in Various Environmental Matrices around a Manufacturing Plant in China. *Environ. Sci. Technol.* **2012**, *46*, 13136–13143. [[CrossRef](#)] [[PubMed](#)]
- Mu, X.; Huang, Y.; Li, X.; Lei, Y.; Teng, M.; Li, X.; Wang, C.; Li, Y. Developmental Effects and Estrogenicity of Bisphenol A Alternatives in a Zebrafish Embryo Model. *Environ. Sci. Technol.* **2018**, *52*, 3222–3231. [[CrossRef](#)] [[PubMed](#)]
- Choi, Y.J.; Lee, L.S. Partitioning Behavior of Bisphenol Alternatives BPS and BPAF Compared to BPA. *Environ. Sci. Technol.* **2017**, *51*, 3725–3732. [[CrossRef](#)]
- Liu, Y.; Zhang, X.; Wu, F. Photodegradation of bisphenol AF in montmorillonite dispersions: Kinetics and mechanism study. *Appl. Clay Sci.* **2010**, *49*, 182–186. [[CrossRef](#)]

8. Yang, T.; Wang, L.; Liu, Y.; Huang, Z.; He, H.; Wang, X.; Jiang, J.; Gao, D.; Ma, J. Comparative study on ferrate oxidation of BPS and BPAF: Kinetics, reaction mechanism, and the improvement on their biodegradability. *Water Res.* **2019**, *148*, 115–125. [[CrossRef](#)]
9. Wang, Q.; Zeng, H.; Liang, Y.; Cao, Y.; Xiao, Y.; Ma, J. Degradation of bisphenol AF in water by periodate activation with FeS (mackinawite) and the role of sulfur species in the generation of sulfate radicals. *Chem. Eng. J.* **2021**, *407*, 126738. [[CrossRef](#)]
10. Li, W.; Zhang, Y.; Cheng, X.; Wang, J.; Yang, B.; Guo, H. Amino-modified metal–organic frameworks as peroxymonosulfate catalyst for bisphenol AF decontamination: ROS generation, degradation pathways, and toxicity evaluation. *Sep. Purif. Technol.* **2022**, *282*, 119967. [[CrossRef](#)]
11. Xu, X.; Liu, Q.; Bai, L.; Wang, L.; Wang, D.; Gao, S. Transformation of Bisphenol AF during Aqueous Chlorination: Kinetics, Mechanisms, and Influence of Ph. *ACS EST Water* **2021**, *1*, 449–458. [[CrossRef](#)]
12. Khan, J.A.; He, X.; Shah, N.S.; Khan, H.M.; Hapeshi, E.; Fatta-Kassinos, D.; Dionysiou, D.D. Kinetic and mechanism investigation on the photochemical degradation of atrazine with activated  $H_2O_2$ ,  $S_2O_8^{2-}$  and  $HSO_5^-$ . *Chem. Eng. J.* **2014**, *252*, 393–403. [[CrossRef](#)]
13. Kilic, M.Y.; Abdelraheem, W.H.; He, X.; Kestioglu, K.; Dionysiou, D.D. Photochemical treatment of tyrosol, a model phenolic compound present in olive mill wastewater, by hydroxyl and sulfate radical-based advanced oxidation processes (AOPs). *J. Hazard. Mater.* **2019**, *367*, 734–742. [[CrossRef](#)] [[PubMed](#)]
14. Sajjadi, S.; Khataee, A.; Bagheri, N.; Kobya, M.; Şenocak, A.; Demirbas, E.; Karaoğlu, A.G. Degradation of diazinon pesticide using catalyzed persulfate with  $Fe_3O_4@MOF-2$  nanocomposite under ultrasound irradiation. *J. Ind. Eng. Chem.* **2019**, *77*, 280–290. [[CrossRef](#)]
15. Lei, Y.; Tian, Y.; Fang, C.; Zhan, W.; Duan, L.; Zhang, J.; Zuo, W.; Kong, X. Insights into the oxidation kinetics and mechanism of diesel hydrocarbons by ultrasound activated persulfate in a soil system. *Chem. Eng. J.* **2019**, *378*, 122253. [[CrossRef](#)]
16. Bruton, T.A.; Sedlak, D.L. Treatment of perfluoroalkyl acids by heat-activated persulfate under conditions representative of in situ chemical oxidation. *Chemosphere* **2018**, *206*, 457–464. [[CrossRef](#)]
17. Yang, L.; Xue, J.; He, L.; Wu, L.; Ma, Y.; Chen, H.; Li, H.; Peng, P.; Zhang, Z. Review on ultrasound assisted persulfate degradation of organic contaminants in wastewater: Influences, mechanisms and prospective. *Chem. Eng. J.* **2019**, *378*, 122146. [[CrossRef](#)]
18. Guo, H.; Ke, T.; Gao, N.; Liu, Y.; Cheng, X. Enhanced degradation of aqueous norfloxacin and enrofloxacin by UV-activated persulfate: Kinetics, pathways and deactivation. *Chem. Eng. J.* **2017**, *316*, 471–480. [[CrossRef](#)]
19. Huang, Y.; Sun, Y.; Xu, Z.; Luo, M.; Zhu, C.; Li, L. Removal of aqueous oxalic acid by heterogeneous catalytic ozonation with MnOx/sewage sludge-derived activated carbon as catalysts. *Sci. Total Environ.* **2017**, *575*, 50–57. [[CrossRef](#)]
20. Qian, L.; Kopinke, F.; Scherzer, T.; Griebel, J.; Georgi, A. Enhanced degradation of perfluorooctanoic acid by heat-activated persulfate in the presence of zeolites. *Chem. Eng. J.* **2022**, *429*, 132500. [[CrossRef](#)]
21. Li, Y.; Sun, J.; Sun, S.P.  $Mn^{2+}$ -mediated homogeneous Fenton-like reaction of Fe(III)-NTA complex for efficient degradation of organic contaminants under neutral conditions. *J. Hazard. Mater.* **2016**, *313*, 193–200. [[CrossRef](#)] [[PubMed](#)]
22. Yang, W.; Li, X.; Jiang, Z.; Li, C.; Zhao, J.; Wang, H.; Liao, Q. Structure-dependent catalysis of  $Co_3O_4$  crystals in persulfate activation via nonradical pathway. *Appl. Surf. Sci.* **2020**, *525*, 146482. [[CrossRef](#)]
23. Avetta, P.; Pensato, A.; Minella, M.; Malandrino, M.; Maurino, V.; Minero, C.; Hanna, K.; Vione, D. Activation of Persulfate by Irradiated Magnetite: Implications for the Degradation of Phenol under Heterogeneous Photo-Fenton-Like Conditions. *Environ. Sci. Technol.* **2015**, *49*, 1043–1050. [[CrossRef](#)]
24. Zhang, J.; Chen, M.; Zhu, L. Activation of persulfate by  $Co_3O_4$  nanoparticles for orange G degradation. *RSC Adv.* **2016**, *6*, 758–768. [[CrossRef](#)]
25. Wang, S.; Wang, J. Bimetallic and nitrogen Co-doped biochar for peroxymonosulfate (PMS) activation to degrade emerging contaminants. *Sep. Purif. Technol.* **2023**, *307*, 122807. [[CrossRef](#)]
26. Jiang, Z.; Li, Y.; Zhou, Y.; Liu, X.; Wang, C.; Lan, Y.; Li, Y.  $Co_3O_4-MnO_2$  nanoparticles moored on biochar as a catalyst for activation of peroxymonosulfate to efficiently degrade sulfonamide antibiotics. *Sep. Purif. Technol.* **2022**, *281*, 119935. [[CrossRef](#)]
27. Chen, X.; Li, F.; Zhang, M.; Liu, B.; Chen, H.; Wang, H. Highly dispersed and stabilized  $Co_3O_4/C$  anchored on porous biochar for bisphenol A degradation by sulfate radical advanced oxidation process. *Sci. Total Environ.* **2021**, *777*, 145794. [[CrossRef](#)] [[PubMed](#)]
28. Su, Y.; Zheng, X.; Cheng, H.; Rao, M.; Chen, K.; Xia, J.; Lin, L.; Zhu, H. Mn- $Fe_3O_4$  nanoparticles anchored on the urushiol functionalized 3D-graphene for the electrochemical detection of 4-nitrophenol. *J. Hazard. Mater.* **2021**, *409*, 124926. [[CrossRef](#)]
29. Li, X.; Niu, C.; Huang, D.; Wang, X.; Zhang, X.; Zeng, G.; Niu, Q. Preparation of magnetically separable  $Fe_3O_4/BiOI$  nanocomposites and its visible photocatalytic activity. *Appl. Surf. Sci.* **2013**, *286*, 40–46. [[CrossRef](#)]
30. Bao, S.; Yan, N.; Shi, X.; Li, R.; Chen, Q. High and stable catalytic activity of porous Ag/ $Co_3O_4$  nanocomposites derived from MOFs for CO oxidation. *Appl. Catal. A Gen.* **2014**, *487*, 189–194. [[CrossRef](#)]
31. Qin, C.; Qi, Y.; Teng, X.; Ajarem, J.S.; Allam, A.A.; Qu, R. Degradation of Bisphenol AF (BPAF) by zero-valent iron activated persulfate: Kinetics, mechanisms, theoretical calculations, and effect of co-existing chloride. *Chemosphere* **2023**, *316*, 137774. [[CrossRef](#)]
32. Chen, W.; Huang, J.; Yu, X.; Fu, X.; Zhu, Y.; Zhang, Y. The roles of graphene and sandwich structure in rGO/BiOI/rGO to enhance the photoelectrocatalytic activity. *J. Solid State Chem.* **2020**, *289*, 121480. [[CrossRef](#)]
33. Xiong, J.; Zeng, H.; Xu, S.; Peng, J.; Liu, F.; Wang, L. Enhancing the intrinsic properties of flower-like BiOI by S-doping toward excellent photocatalytic performances. *J. Mater. Sci. Technol.* **2022**, *118*, 181–189. [[CrossRef](#)]



34. Tang, W.; Zhang, Y.; Guo, H.; Liu, Y. Heterogeneous activation of peroxymonosulfate for bisphenol AF degradation with  $\text{BiOI}_{0.5}\text{Cl}_{0.5}$ . *RSC Adv.* **2019**, *9*, 14060–14071. [[CrossRef](#)] [[PubMed](#)]
35. Malefane, M.E.; Feleni, U.; Mafa, P.J.; Kuvarega, A.T. Fabrication of direct Z-scheme  $\text{Co}_3\text{O}_4/\text{BiOI}$  for ibuprofen and trimethoprim degradation under visible light irradiation. *Appl. Surf. Sci.* **2020**, *514*, 145940. [[CrossRef](#)]
36. Song, Y.; Qi, J.; Tian, J.; Gao, S.; Cui, F. Construction of  $\text{Ag}/\text{g-C}_3\text{N}_4$  photocatalysts with visible-light photocatalytic activity for sulfamethoxazole degradation. *Chem. Eng. J.* **2018**, *341*, 547–555. [[CrossRef](#)]
37. Liang, C.; Wang, Z.; Mohanty, N. Influences of carbonate and chloride ions on persulfate oxidation of trichloroethylene at 20 °C. *Sci. Total Environ.* **2006**, *370*, 271–277. [[CrossRef](#)]
38. Wu, C.; Linden, K.G. Phototransformation of selected organophosphorus pesticides: Roles of hydroxyl and carbonate radicals. *Water Res.* **2010**, *44*, 3585–3594. [[CrossRef](#)] [[PubMed](#)]
39. Wang, Q.; Cao, Y.; Zeng, H.; Liang, Y.; Ma, J.; Lu, X. Ultrasound-enhanced zero-valent copper activation of persulfate for the degradation of bisphenol AF. *Chem. Eng. J.* **2019**, *378*, 122143. [[CrossRef](#)]
40. Wang, Z.; Wang, Z.; Li, W.; Lan, Y.; Chen, C. Performance comparison and mechanism investigation of  $\text{Co}_3\text{O}_4$ -modified different crystallographic  $\text{MnO}_2$  ( $\alpha$ ,  $\beta$ ,  $\gamma$ , and  $\delta$ ) as an activator of peroxymonosulfate (PMS) for sulfisoxazole degradation. *Chem. Eng. J.* **2022**, *427*, 130888. [[CrossRef](#)]
41. Quang, N.D.; Majumder, S.; Van, P.C.; Jeong, J.; Kim, C.; Kim, D.  $\text{Co}_3\text{O}_4$ /reduced graphene oxide/ $\text{BiVO}_4$  nanorod as high performance photoanode for water oxidation. *Electrochim. Acta* **2020**, *364*, 137283. [[CrossRef](#)]
42. Ren, Y.; Lin, L.; Ma, J.; Yang, J.; Feng, J.; Fan, Z. Sulfate radicals induced from peroxymonosulfate by magnetic ferrosphenel  $\text{MFe}_2\text{O}_4$  ( $\text{M} = \text{Co}, \text{Cu}, \text{Mn}, \text{and Zn}$ ) as heterogeneous catalysts in the water. *Appl. Catal. B Environ.* **2015**, *165*, 572–578. [[CrossRef](#)]
43. Yang, Q.; Choi, H.; Dionysiou, D.D. Nanocrystalline cobalt oxide immobilized on titanium dioxide nanoparticles for the heterogeneous activation of peroxymonosulfate. *Appl. Catal. B Environ.* **2007**, *74*, 170–178. [[CrossRef](#)]
44. Zhang, L.; Yang, X.; Han, E.; Zhao, L.; Lian, J. Reduced graphene oxide wrapped  $\text{Fe}_3\text{O}_4\text{-Co}_3\text{O}_4$  yolk-shell nanostructures for advanced catalytic oxidation based on sulfate radicals. *Appl. Surf. Sci.* **2017**, *396*, 945–954. [[CrossRef](#)]
45. Anipsitakis, G.P.; Dionysiou, D.D. Radical Generation by the Interaction of Transition Metals with Common Oxidants. *Environ. Sci. Technol.* **2004**, *38*, 3705–3712. [[CrossRef](#)]
46. Wang, Y.; Indrawirawan, S.; Duan, X.; Sun, H.; Ang, H.M.; Tade, M.O.; Wang, S. New insights into heterogeneous generation and evolution processes of sulfate radicals for phenol degradation over one-dimensional  $\alpha\text{-MnO}_2$  nanostructures. *Chem. Eng. J.* **2015**, *266*, 12–20. [[CrossRef](#)]
47. Li, X.; Liu, J.; Rykov, A.I.; Han, H.; Jin, C.; Liu, X.; Wang, J. Excellent photo-Fenton catalysts of Fe–Co Prussian blue analogues and their reaction mechanism study. *Appl. Catal. B Environ.* **2015**, *179*, 196–205. [[CrossRef](#)]

**Disclaimer/Publisher’s Note:** The statements, opinions and data contained in all publications are solely those of the individual author(s) and contributor(s) and not of MDPI and/or the editor(s). MDPI and/or the editor(s) disclaim responsibility for any injury to people or property resulting from any ideas, methods, instructions or products referred to in the content.